Formation mechanism and properties of CdS-Ag$_2$S nanorod superlattices

Denis O. Demchenko[1], Richard D. Robinson[2], Bryce Sadtler[3],
Can K. Erdonmez[3], A. Paul Alivisatos[2,3], and Lin-Wang Wang[1]

[1]*Computational Research Division, Lawrence Berkeley National Laboratory, Berkeley, California 94720*
[2]*Materials Science Division, Lawrence Berkeley National Laboratory, Berkeley, California 94720*
[3]*Department of Chemistry, University of California, Berkeley, California 94720*
(Dated: October 23, 2007)

The mechanism of formation of recently fabricated CdS-Ag$_2$S nanorod superlattices is considered and their elastic and electronic properties are predicted theoretically based on experimental structural data. We consider different possible mechanisms for the spontaneous ordering observed in these 1D nanostructures, such as diffusion-limited growth and ordering due to epitaxial strain. A simplified model suggests that diffusion-limited growth can contribute to the observed ordering, but cannot account for the full extent of the ordering alone. Elastic properties of bulk Ag$_2$S are predicted using a first principles method and are fed into a classical valence force field (VFF) model of the nanostructure. The VFF results show significant repulsion between Ag$_2$S segments, strongly suggesting that the interplay between the chemical interface energy and strain due to the lattice mismatch between the two materials drives the spontaneous pattern formation.

I. INTRODUCTION

There has been much recent progress in fabricating one dimensional (1D) superlattices (e.g. Si/SiGe,[1] InAs/InP,[2] and GaAs/GaP[3] superlattice nanowires), stimulated by interest in use of such nanostructures in photonic and thermoelectric applications. The vapor-liquid-solid (VLS) methods typically employed to grow these structures are facile but often yield large feature sizes.[1–3] Adoption of colloidal methods for nanostructure fabrication has the potential advantages of lower costs and achievement of smaller structures with enhanced and tunable quantum confinement effects that can be utilized in optoelectronic devices such as light-emitting diodes and solar cells.[4,5] However, to date, published preparations of 1D superlattices using colloidal growth[6] have been cumbersome with the resulting 1D superlattices, which have only a few layers before the procedure is too difficult.[7] Therefore, instead of relying on sequential methods which require iterated syntheses to produce ordering, it is highly desirable to develop spontaneous ordering methods, where a pattern of nanostructures emerges naturally due to intrinsic interactions on the nanoscale. For instance, in growth of 2D and 3D structures, lattice strain has been used to drive pattern formation on the nanoscale, yielding self-assembled quantum dots and their ordered arrays following epitaxial growth.[8–13] In these experiments, strain fields created by lattice mismatch between the deposited quantum dots (QD) and the substrate (or the overlayer) influence the deposition of subsequent QD layers, leading to formation of vertically ordered QD arrays. Another source of spontaneous pattern formation in semiconductor nanostructures can be diffusion-limited ordering,[14] where, in principle, a regular pattern can form due to slow diffusion of atoms between growing islands.

We recently showed that partial cation exchange can be used to introduce ordered Ag$_2$S segments into CdS nanorods.[15] During cation exchange, dissolved Ag ions displace Cd cations from CdS nanorods also present in solution, resulting in islands of Ag$_2$S in the CdS nanorods. As the reaction progresses, the growing Ag$_2$S islands yield segments spanning the whole nanorod diameter and spontaneously form ordered nanorod superlattices. A transmission electron microscopy (TEM) image of such nanorod superlattices is shown in Fig. 1(a), where a periodic arrangement of the dark Ag$_2$S segments within the nanorods is visible. If excess of Ag$^+$ cations are added, eventually the whole CdS nanorod converts into a Ag$_2$S nanorod, preserving shape and length. If however, only a partial cation exchange is performed, the nanorod superlattices are formed and remain stable dried on a substrate for months. We hypothesized the formation of such spontaneously ordered superlattices to be driven largely by the lattice strain field created at the CdS-Ag$_2$S interfaces (see Ref. 15 for an introduction and brief discussion of these ideas). The strain fields are expected to result in repulsion between Ag$_2$S segments, which, operating in concert with diffusion-limited Ostwald ripening, can yield and stabilize the observed periodic patterns. In this paper, we present more detailed theoretical considerations of the mechanism of formation as well as the structural and elastic properties of the CdS nanorod superlattices.

In the next section, we outline the theoretical methods used. Section III discusses our results, beginning with an overview of the superlattice formation process and proceeding to modeling of the CdS-Ag$_2$S interface. A detailed discussion of a proposed mechanism for spontaneous ordering is presented, along with numerical calculation of the expected strain fields in this system in support of the mechanism. Section IV summarizes our findings.

II. METHODS

The experimental procedure for fabricating CdS-Ag$_2$S nanorod superlattices has been published elsewhere.[15] An image of the nanostructures modeled here is shown in Fig. 1(a), where segments of Ag$_2$S have spontaneously formed within CdS nanorods in a periodic arrangement. In order to theoretically clarify the formation mechanism and properties of these structures, we use a combination of *ab initio* methods as well as the classical valence force field (VFF) method. The first principles calculations of the elastic properties of Ag$_2$S and CdS-Ag$_2$S interfaces and superlattices employed the VASP,[16] and Petot packages.[17] We used the generalized gradient (GGA) as well as local density (LDA) approximations, along with projector augmented wave (PAW) and norm-conserving pseudopotential methods. To study the role that diffusion-limited island growth plays in producing the observed ordering, we employ a simple kinetic model in 1D, which describes Ostwald ripening due to diffusion of atoms between the islands. The VFF model[18] was used to compute the lattice strain fields in the experimental size nanorod superlattices, with parameters obtained from fitting the Ag$_2$S elastic constants obtained from the first principles calculations.

III. RESULTS AND DISCUSSION

A. An Overview of Formation of CdS-Ag$_2$S Nanorod Superlattice

In the partial cation exchange experiments, the initial colloidal CdS nanorods are fabricated to be very smooth with small diameter dispersion (about 10%) with lengths ranging between 30 and 100 nm. The colloidal CdS nanorods are added to a solution of toluene, AgNO$_3$, and methanol at -66°C in air.[15] During the cation exchange reaction, the Ag$^+$ cations substitute for Cd^{2+} cations within the nanorods, due to the preferential binding of MeOH to the divalent Cd^{2+} ion than to Ag$^+$ (here Me stands for a methyl group).[19] This solid-state exchange reaction has been shown to take place on a millisecond timescale[19,20] on the nanoscale due to the small size of the nanocrystals and the high mobilities of Ag$^+$ and Cd^{2+} within the crystalline lattices. The process is facilitated by the fact that both Ag$^+$ and Cd^{2+} are fast diffusers in CdS.[21,22] The concentration of AgNO$_3$ controls the number of Ag$^+$ cations and therefore defines the fraction of Cd^{2+} cations to be exchanged: an excess of Ag$^+$ cations results in complete conversion of the CdS rods into Ag$_2$S.[19] At low Ag$^+$ concentrations, the resulting partial cation exchange reaction produces a random arrangement of Ag$_2$S islands embedded at the nanorod surfaces. At intermediate Ag$^+$ concentrations, the islands appear to have grown larger and into the nanorod interior, due to the additional Ag$^+$ cations as well as the the absorption of smaller islands by larger ones (Ostwald ripening).

As islands grow, at some point, all surviving islands will have come to span the entire nanorod diameter, achieving a cylindrical, low interface energy geometry. This arrangement is expected to be quite stable since further diffusion of Ag$^+$ ions between segments will not change the interface area unless a whole segment is absorbed by the other segments. However, at this point, the elastic repulsion between segments is expected to stabilize the islands against further ripening, as discussed below. Furthermore, since Ag$^+$ is able to easily diffuse throughout the nanorod the segments are mobile, and they move apart to minimize the repulsive strain interaction, thus spontaneously self-ordering. Thus, the periodic pattern of Ag$_2$S segments in the CdS nanorod (Fig. 1(a)) results from a sequence of initial nucleation and ripening followed by elastically-driven local segregation of of mobile Ag$^+$ ions.

B. CdS-Ag$_2$S Epitaxial Attachment

The experimental powder X-ray diffraction (XRD) patterns reveal the superlattices to contain crystalline regions of CdS (of the wurtzite form) and Ag$_2$S (of the monoclinic form). The unit cell of the latter structure is shown in the Fig. 1(b). This monoclinic (low temperature) phase of Ag$_2$S has been studied in the literature[23–25] both theoretically and experimentally. It has been found to be a semiconductor with a measured bandgap ranging from 0.78 to 1.0 eV[25] (0.68 eV calculated within LDA[24]). The sulfur atoms in bulk Ag$_2$S form a slightly distorted bcc lattice with silver atoms occupying octahedral and tetrahedral sites of the sulfur lattice.[24] Considering the high mobility of Ag$^+$ ions, considerable distortions and cation disorder with reference to the bulk structure may be present in the highly strained, high surface area nanorod superlattices.

The fully formed nanorod superlattices exhibit epitaxial attachment of Ag$_2$S and CdS regions. However, epitaxially attaching monoclinic Ag$_2$S to the CdS wurtzite lattice, along the [0001] axis of the nanorod requires significant distortions, particularly of the Ag$_2$S lattice. Since the sulfur atoms in Ag$_2$S form a *bcc* lattice, we can construct a supercell (Fig. 1(c)) directly from the original monoclinic Ag$_2$S unit cell (Fig. 1(b)), where the sulfur atoms corresponding to each other in the two lattices are numbered. This supercell can attach its (001) plane (which is the (110) plane of a *bcc* lattice) to the (0001) wurtzite plane of CdS (Fig. 1(d)), since both have hexagonal symmetry. Such attachment, however causes large distortions of both the Ag$_2$S and CdS lattices: namely, the Ag$_2$S lattice constant, in comparison with that of CdS, is 4% smaller along the [100] supercell axis ([1000] wurtzite) and 15% larger along the [010] supercell axis ([2100] wurtzite). Nevertheless, as noted before,[26,27] high strains in nanorod superlattices can exist without resulting in dislocation formation.
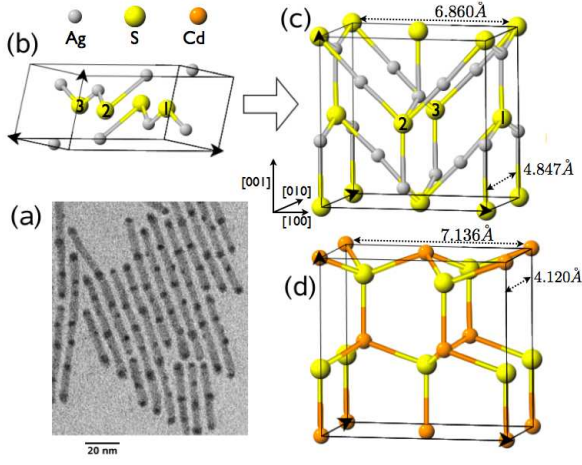
FIG. 1: (color online) (a) Experimental TEM image of CdS-Ag$_2$S nanorod superlattices fabricated by partial cation exchange. The dark regions are the Ag$_2$S segments embedded in the CdS nanorods. (b) Monoclinic phase of Ag$_2$S unit cell matching the experimental XRD data (corresponding to Table I). (c) Orthorhombic Ag$_2$S supercell, built from monoclinic unit cells (b), used to epitaxially attach to wurtzite CdS in the [0001] direction (d). The numbered atoms in (b) and (c) show the construction of the orthorhombic cell from the monoclinic unit cell. In order to epitaxially attach, both CdS and Ag$_2$S must distort. The lattice mismatch between wurtzite CdS and the orthorhombic supercell of Ag$_2$S is +4% tension along the [100] Ag$_2$S supercell axis ([1000] wurtzite) and -15% compression along the [010] Ag$_2$S supercell axis ([2100] wurtzite). This creates large strain when both lattices distort, relaxing into the lowest energy geometry.

In order to confirm the crystal structure we have simulated the XRD pattern expected from a powder mixture of Ag$_2$S nanocubes and CdS nanorods. Several nanorod and nanocube sizes were considered. In Fig. 2, we show the measured XRD spectrum (Fig. 2(a)) along with the patterns computed for 5.3×11 nm CdS nanorods and Ag$_2$S cubes with sides of 10×10 nm, 5×5 nm, and 2.5×2.5 nm (Fig. 2(b,c,d, respectively)). For a given geometry, all pairwise atomic distances, r_{ij}, were computed. Then, the XRD intensity pattern can be obtained as

$$I(S) \propto \frac{F_i(S)F_j(S)}{S} \sum_{i \neq j} \frac{\sin(2\pi r_{ij}S)}{r_{ij}}, \quad (1)$$

where, $S = 2\sin(\Theta)/\lambda$ is a scattering parameter, $I(S)$ is the computed intensity, Θ is the angle of diffraction, λ is the wavelength of incident X-rays, and $F_k(S)$ is the atomic structure factor for the k-th atom in the nanostructure. We find a good qualitative agreement with the experimental pattern for the wurtzite structure of CdS, and the monoclinic structure of Ag$_2$S listed in Table I. The best match is for 5.3×11 nm CdS nanorods and 5×5 nm Ag$_2$S nanocubes, which corresponds to the experimental nanorod diameters with an average center-to-center separation of 16 nm between Ag$_2$S segments. The Ag$_2$S peaks in the experimental data are broader
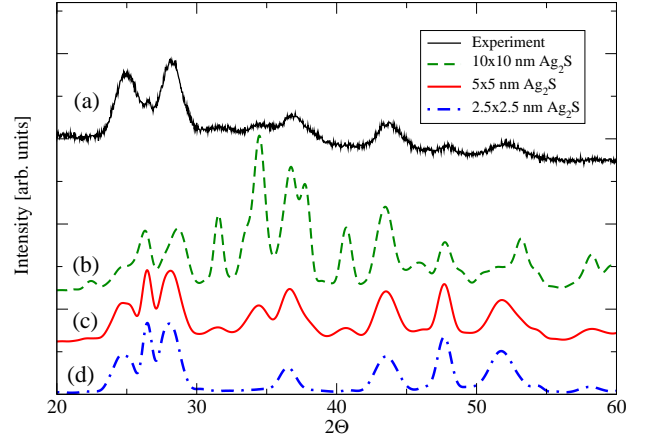

FIG. 2: (color online) The experimental XRD diffraction pattern from CdS-Ag$_2$S nanorod superlattices (black line) and three simulated XRD patterns. The simulated patterns are obtained by summing the pattern predicted for 5.3×11 nm CdS nanorods with the predicted pattern for Ag$_2$S cubes with sides of 5×5 nm (thick red line), 10×10 nm (dashed green line), and 2.5×2.5 nm (dash-dotted blue line). The simulation is performed for the Ag$_2$S structure described in Table I and Fig. 1(b). The case of 5×5 nm Ag$_2$S cubes qualitatively matches the experiment. Ag$_2$S peaks are broader in experimental data due to the presence of strain created by the CdS-Ag$_2$S interfaces.

than the computed ones, possibly due to strain created at the CdS-Ag$_2$S interfaces, which was not included in this calculation. The Ag$_2$S structure listed in Table I is similar to the previously reported structural data of bulk Ag$_2$S, but with slightly different Ag atoms positions.

The large strains are likely a key requirement for the formation of the periodic pattern observed in nanorod superlattices. As we show here, the strain fields created by this lattice mismatch at the interface lead to a repulsive interaction between adjacent Ag$_2$S segments. This repulsion, coupled with the segments' mobility leads to ordering of segments, and stabilization of the structure.

C. Interface Formation Energy

During the initial stages of growth, when Ostwald ripening is dominant, the larger regions of Ag$_2$S absorb smaller islands. The direction of the process is determined by the interface formation energy, which is the energy difference between the CdS-Ag$_2$S interface and the corresponding Ag$_2$S and CdS bulk structures. A positive interface formation energy will result in Ostwald ripening, merging smaller islands into larger ones to a lower surface area, and thus lower the total energy. In order to clarify this, we calculated the CdS-Ag$_2$S interface formation energy in the supercell geometry constructed as in Fig. 1(c,d). The CdS and Ag$_2$S slab sizes were 19.4 Å and 15.2 Å, respectively, in the z-direction of the supercell, and infinite in the xy plane. The structure was

TABLE I: Crystal data of monoclinic phase of Ag$_2$S. The modeled XRD pattern for this structure matches the experimental XRD pattern of Ag$_2$S segments in the formed CdS-Ag$_2$S nanorod superlattice.

(a) Lattice parameters (in Å) and angle

a	b	c	β
4.231	6.93	9.526	125.29°

(b) Atomic positions

Atom	x	y	z
S	0.5	0.7383	0.3694
S	0.5	0.7617	0.8694
S	0.5	0.2617	0.6306
S	0.5	0.2383	0.1306
Ag	0.0712	0.0169	0.3075
Ag	0.7259	0.3213	0.4362
Ag	0.9288	0.5169	0.1925
Ag	0.9288	0.9831	0.6925
Ag	0.0712	0.4831	0.8075
Ag	0.2741	0.8213	0.0638
Ag	0.2741	0.6787	0.5638
Ag	0.7259	0.1787	0.9362

relaxed with respect to internal degrees of freedom, lattice parameters in xy plane, and the distance between slabs. The interface formation energy computed from the *ab initio* total energies is given by

$$E_{form} = E_t - \sum_i N_i \mu_i. \qquad (2)$$

Here, E_t is the total energy of the supercell, N_i is the number of atoms of the type i in the cell, and μ_i is the chemical potential of the i-th atom. The supercell was large enough so the interaction between the two adjacent interfaces is negligible. Our first principles calculations result in a CdS-Ag$_2$S interface formation energy of $+1.68$ eV per primitive interface containing one Cd-S-Ag unit. Therefore, it is energetically favorable to merge small islands into large ones. A critical size is reached when an island spans the entire nanorod diameter, forming an Ag$_2$S segment. In this case, exchange of atoms between formed segments does not change the Ag$_2$S segment surface area and surface energy.

D. Diffusion

Pattern formation in systems away from equilibrium has been extensively studied in the past.[28] In reaction-diffusion systems, a pattern can form due to a Turing instability: a solution which is stable and uniform in the absence of diffusion becomes unstable and produces patterns when conditions are altered to allow diffusion.[29]

During the formation of CdS-Ag$_2$S nanorod superlattices, the reaction-diffusion system is out of equilibrium and results in periodic patterns with intrinsic wavelengths which are longer than (and consequently, dependent upon) the physical dimensions of the system, i.e., the nanorod diameter. Within this viewpoint, the involvement of a Turing instability in the evolution of CdS-Ag$_2$S nanorod superlattice appears possible. However, the observed nucleation and ripening does not seem to be qualitatively consistent with a Turing instability. During a reaction displaying a Turing instability, a final pattern appears from the beginning, with its amplitude increasing with time. Meanwhile, assuming that the structures obtained at different concentrations also correspond to different stages in the evolution of the superlattices at a fixed concentration, islands appear to ripen and the segments appear to be mobile. In addition, the initial distribution of Ag$_2$S regions does not show periodicity. Thus, the pattern of segments seems to change until a periodic spacing of islands is achieved and the observed ordering does not support a Turing model.

Spontaneous ordering on the nanoscale due to limited diffusion of adatoms has been studied in the past. Concerning 3D systems, several theories of kinetic ordering of islands have been proposed.[30] (Also see Ref. 8, and references therein). They might be adequate only at the initial stages of growth, since they ignore the influence of strain created by islands on the diffusion of atoms, which was pointed out to be important in 2D and 3D island growth.[31] The possibility of producing ordered patterns solely due to diffusion limited aggregation in 1D has been addressed theoretically,[14] where modeling the deposition of particles along a line results in regular patterns.

Here, we study this possibility in 1D by modeling the diffusion of Ag atoms between islands and ripening of islands at the expense of each other. Initially, islands of Ag$_2$S are randomly distributed along a 1D array, and are assigned random small sizes. Inside the CdS solid, there is a small number of free Ag atoms, which reach near-equilibrium with the Ag$_2$S islands. Islands can lose or gain Ag atoms from the CdS solid, and a representation of this process is allowed in the numerical model with the direction of the process defined by the energy balance described below.

We model the nanorod as an array of sites, here i is indexing all sites in CdS host, while l is indexing islands, $i(l)$ is the site index of the l-th island. The energy cost to add one Ag atom to the l-th island located at the $i(l)$-th site is approximated by the expression

$$\Delta E_l = -E_{Ag} + \beta m_l^{-1/3} - kT \ln\left[\frac{x_{i(l)}}{(1-x_{i(l)})}\right] \qquad (3)$$

where, m_l is the number of atoms in the l-th island, $x_{i(l)}$ is the concentration of Ag atoms at the $i(l)$-th site, E_{Ag} is Ag$_2$S chemical formation energy (compared to free Ag atoms in CdS), and β is a constant that dictates the magnitude of the interfacial energy. The first term, $-E_{Ag}$ is negative, corresponding to the observation that segrega-

tion of Ag$^+$ into Ag$_2$S islands appears to be favorable. The last term is the entropy of a mixture of Ag atoms in the CdS solid that depends on temperature, kT, and the Ag atoms concentration x_i. If the energy, ΔE_l, is negative then it is favorable for the l-th island (at i-th site) to absorb Ag atoms, if it is positive then this island will lose atoms. We also set the second term in Eq. 3 to zero after an island reaches some critical mass, for when the segment is fully formed, spanning the whole nanorod diameter, the exchange of atoms with the environment results in no change of the surface energy.

The model evolves with time according to the following three equations. The first two equations,

$$x_{i(l)}(t+1) = x_{i(l)}(t) \pm \alpha x_{i(l)} e^{-\frac{E_b}{kT}} \qquad (4)$$

$$m_l(t+1) = m_l(t) \mp \alpha x_{i(l)} e^{-\frac{E_b}{kT}} \qquad (5)$$

describe the exchange of Ag atoms between the islands m_l and the CdS solid x_i at $i(l)$-th site. Here the concentration of Ag atoms in the CdS solid, x_i, is increasing (i.e. choosing + sign in Eq. 4 and − sign in Eq. 5) if ΔE_l is positive. This corresponds to an island losing atoms to the CdS, increasing its concentration by an amount proportional to α. We assume the energy activation barrier, E_b, to leave the island into the CdS matrix is independent of the island size, therefore adding a value proportional to Ag atom concentration $x_{i(l)}$ at a given temperature. The direction is reversed if ΔE_l is negative. The process is mediated by the diffusion of Ag atoms in the CdS defined by gradients of concentration x_i

$$x_i(t+1) = x_i(t) + D\left[x_{i+1}(t) + x_{i-1}(t) - 2x_i(t)\right] \qquad (6)$$

where D is the diffusion coefficient. The conservation of mass is enforced by limiting the diffusion direction at the boundaries toward the center of the rod. The parameters are chosen to model the experimental conditions and results, i.e., formation of islands, ripening, and maintaining a low concentration of Ag in the CdS matrix. This is primarily achieved by choosing an optimal $\alpha/De^{-\frac{E_b}{kT}}$ ratio, which controls the diffusion and ripening rates. The term ΔE_l is only indicating the direction of the ripening process for a given island, and its values are unimportant. The CdS solid and the islands reach thermodynamic quasi-equilibrium between islands and their surrounding x_i very quickly. Then the smaller islands slowly lose atoms to bigger islands, since the second term in the Eq. 3 favors larger islands. Eventually, larger islands absorb the smaller islands entirely modeling the Ostwald ripening, and reach the critical size m_c, beyond which the segment is formed and the second term in Eq. 3 disappears.

Typical results of the modeling are shown in Figure 3, where we show the island weight and position on a typical 50 nm long nanorod. Initially, island were distributed randomly along the 1D nanorod and assigned small random sizes. The simulation then demonstrates
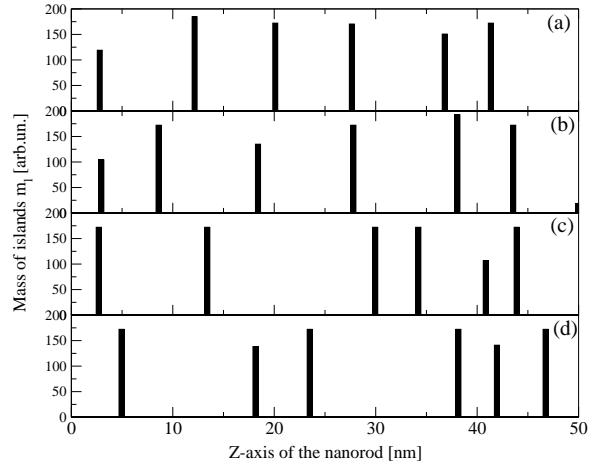

FIG. 3: The islands initially randomly formed in the one dimensional rod. The growth of the larger islands at the expense of the smaller islands (i.e. Ostwald ripening) leads to the formation of ordered islands due to diffusion. The length of bars shows the relative number of Ag atoms in an island situated along the long axis of the nanorod (horizontal axis of the plot). The critical island size is $m_c = 100$. The panels (a), (b), (c), (d) show four different results of modeling for different initial random distributions of small islands. Diffusion alone is producing somewhat ordered islands, but the ordering is typically poor. The results presented here are typical for diffusion-limited ordering. Panels (a) and (b) show relatively ordered patterns, while (c) and (d) are rather disordered, all patterns have similar probabilities of forming, showing poor ordering solely due to diffusion.

behavior typical for Ostwald ripening, where larger islands grow at the expense of the smaller islands. The four panels show the resulting patterns after the Ostwald ripening is finished. All the islands have reached critical sizes where the energy balance will not change as a result of Ag exchange between islands. Figure 3, presenting a typical diffusion limited ordering scenario, shows that the islands are ordered poorly. Running a number of simulations for the geometry considered, even in somewhat ordered cases shown in panels (a) and (b), there are always a few large islands located close to each other. In addition, equally probable are the cases where the ordering is very poor, as shown in Fig. 3 (c) and (d). Therefore, if spontaneous ordering were driven by diffusion alone, we would expect experiments to produce rods with several out-of-place Ag$_2$S segments in practically every nanorod. In addition, a large number of fairly disordered nanorods would be expected. That, however, is not the case; experimentally, Ag$_2$S segments are very well ordered (Fig. 1(a)), indicating that diffusion-limited growth alone does not account for the formation of the CdS-Ag$_2$S nanorod superlattices. In order to produce such an ordered state, there must exist a repulsive interaction between the fully formed CdS-Ag$_2$S segments, which drives them apart. (The Ag$_2$S segments are mobile due to the exchange between Ag and Cd ions).

E. Strain

As established above, the nanorod superlattice formation mechanism, which results in a regular Ag_2S segment pattern, implies a repulsive interaction between mobile segments. Among possible candidates for such interaction are *(i)* direct Coulomb repulsion, *(ii)* dipole-dipole interaction, and *(iii)* interaction due to strain. We address and discount the first two of these possibilities below.

(i) The Ag_2S segments exhibit photoluminescence (blue shifted due to quantum confinement[15]), indicating no large number of dangling bond states in the band gap. This, along with TEM images and XRD data, indicate a well formed Ag_2S crystal, which is expected to be charge neutral. Therefore, direct Coulomb repulsion between Ag_2S segments is unlikely.

(ii) To estimate the possible dipole-dipole interaction, we have performed *ab initio* calculations for CdS-Ag_2S superlattices with alternating Ag_2S and CdS slabs in the z-direction and infinite cross section in xy-directions. We used 30 Å thick Ag_2S slabs (9 atomic layers) and the 42 Å thick slabs (12 atomic layers) of CdS. The lattice and the atoms in the 3 layers adjacent to the interfaces were relaxed. The results of the calculation give an electrostatic potential gradient inside the Ag_2S slabs of the superlattice, from which a dipole moment can be deduced. For an experimental nanorod of 4.8 nm diameter and Ag_2S segment of 3 nm length, it yields a dipole moment of approximately 290 Debye. If the symmetry of the lattice in the neighboring segments is the same, these dipole moments will point in the same direction. This interaction, first of all, cannot be used as an ordering mechanism, as it is attractive; secondly, its magnitude is very small (0.04 eV).

(iii) Due to a very large lattice mismatch, significant strain fields are created inside the nanorod. Therefore, the strain is a likely candidate for the repulsive interaction in CdS-Ag_2S nanorod superlattice. Using a VFF model and the elastic parameters, we explain and quantify this repulsion force between the Ag_2S segments.

In order to study the strain and elastic properties of the CdS-Ag_2S nanorod superlattices, we first calculate the elastic constants of the Ag_2S using *ab initio* methods. Although the orthorhombic supercell technically has nine independent elastic constants, in the case of the Ag_2S lattice attachment to wurtzite shown in Fig. 1(c,d) the distortions the Ag_2S lattice undergoes are mainly due to orthogonal uniaxial strain. Thus the shear elastic constants c_{44}, c_{55}, and c_{66} may be neglected in a basic treatment of the distortions, and therefore were not fitted. We only need the six remaining elastic constants c_{11}, c_{22}, c_{33}, c_{12}, c_{13}, and c_{23}. We relax the atomic structure of the Ag_2S unit, apply a small (within a few percent) strains δ_i to the equilibrium lattice and compute the resulting total energies (following Ref. 32). The total energy, assuming linear elasticity up to the limits of distortions, is fitted into a second order expansion in powers of strain tensor components around the equilibrium energy E_0:

$$E(\delta) = E_0 + \tfrac{1}{2}V_0 \sum_{ij} c_{ij}\delta_i\delta_j + O[\delta^3], \qquad (7)$$

where, V_0 is equilibrium volume. We need only consider diagonal strain tensor $\underline{e}$ (with three diagonal components e_1, e_2, e_3), so we apply distortions to the primitive vectors $\mathbf{a_i}$ transforming them as

$$\begin{pmatrix} \mathbf{a_1'} \\ \mathbf{a_2'} \\ \mathbf{a_3'} \end{pmatrix} = \begin{pmatrix} \mathbf{a_1} \\ \mathbf{a_2} \\ \mathbf{a_3} \end{pmatrix} \cdot (\underline{I} + \underline{e}) \qquad (8)$$

($\underline{I}$ is the 3×3 identity matrix) fitting the total energy curves into Eq. 7 and extracting the coefficients at the second order term. To find the elastic constants c_{11}, c_{22}, and c_{33}, three linear tetragonal distortions are applied to the lattice with the strain tensor components equaling, respectively,

$$e_1 = \delta_1, e_2 = e_3 = 0, \qquad (9)$$

$$e_2 = \delta_2, e_1 = e_3 = 0, \qquad (10)$$

and

$$e_3 = \delta_3, e_1 = e_2 = 0. \qquad (11)$$

To find elastic constants c_{12}, c_{13}, and c_{23}, the orthorhombic strains are applied by using distortion matrices $(\underline{I} + \underline{e})\gamma$ and strain tensor components

$$e_1 = \delta_1, e_2 = -\delta_1, e_3 = 0, \gamma = (1 - \delta_1^2)^{-1/3} \qquad (12)$$

$$e_1 = \delta_2, e_2 = 0, e_3 = -\delta_2, \gamma = (1 - \delta_2^2)^{-1/3} \qquad (13)$$

and

$$e_1 = 0, e_2 = \delta_3, e_3 = -\delta_3, \gamma = (1 - \delta_3^2)^{-1/3}. \qquad (14)$$

The resulting elastic constants are listed in the Table II. We feed these bulk elastic constants into the VFF

TABLE II: Elastic constants c_{ij} (using Voigt notation) of orthorhombic cell of Ag_2S in units of $[10^{11}$ dyne/cm$^2]$ from first principles GGA calculations. We also list experimental[33] elastic constants of CdS for comparison.

	Reference	c_{11}	c_{22}	c_{33}	c_{12}	c_{13}	c_{23}
Ag_2S	Present	8.02	9.76	11.57	2.59	3.49	4.36
CdS	Experiment[33]	8.57		9.36	5.21	4.61	

calculation for a nanostructure with a realistic number of atoms in order to study the influence of strain on the lattice mismatched nanorod superlattices.

The VFF model[18,34] is a classical atomistic model for atomic relaxation which treats atoms as points connected by elastic bonds, and in our implementation[34] takes into

account bond stretching and bond angle bending but not bond breaking. The VFF strain energy functional is written in terms of atomic positions $\mathbf{R}_i$ and their elastic interaction with the nearest neighbors only, within a harmonic approximation:

$$E = \frac{3}{16} \sum_i \left\{ \sum_j^{nn} \frac{\alpha_{ij}}{d_{ij}^2} \left[\Delta \mathbf{R}_{ij}^2 - d_{ij}^2 \right]^2 + \right.$$

$$\left. \sum_{j,k>j}^{nn} \frac{\beta_{ijk}}{d_{ij}d_{ik}} \left[\Delta \mathbf{R}_{ij} \cdot \Delta \mathbf{R}_{ik} - d_{ij}d_{ik} \cos \theta_{ijk} \right]^2 \right\}, \quad (15)$$

where, $\Delta \mathbf{R}_{ij} = \mathbf{R}_j - \mathbf{R}_i$, d_{ij} is the ideal bond length between the i-th and j-th atom, θ_{ijk} is the ideal bond angle, and α_{ij} and β_{ijk} are the elastic constants of the model which are fitted to the elastic constants of the bulk Ag_2S and CdS. The summation over j and k indices is performed over nearest neighbors only, while index i runs over all atoms in the nanostructure. The elastic constants α and β can be found from constants c_{ij},[34] computed from first principles for Ag_2S and fitted to experiment for CdS, and are (in units of $[10^3$ dyne/cm]) $\alpha = 29.60$ and $\beta = 9.23$ for Ag_2S, and $\alpha = 26.57$ and $\beta = 4.76$ for CdS. For a given nanostructure, the energy functional of Eq. 15 is minimized with respect to $\{\mathbf{R}_i\}$, yielding the atomic structure that has the lowest elastic energy for a given arrangement of atoms.

In the geometry studied here, the CdS-Ag_2S interface has a lattice mismatch which is different in the x and y directions, as discussed in Section IIIB (Fig. 1). Therefore, upon VFF relaxation, a nanorod will expand and contract along two perpendicular radial directions. We performed VFF calculations for CdS nanorod superlattices with diameters of 4.8 nm and 6 nm, which have two 4 nm thick Ag_2S segments at varying separations. The surfaces of the nanorods were passivated.[35] The rod lengths varied with the segment separation from 30 nm to 42 nm, keeping the distances between segments and nanorod ends constant in order to fix any possible rod end contribution to the elastic energy. The number of atoms in studied structures ranged from 25228 to 57201.

The resulting elastic energies as functions of the segments separation are shown in Figure 4, for a 6 nm diameter nanorod (a), and a 4.8 nm diameter nanorod (b). The elastic energies decrease with increasing separation between the segments indicating elastic repulsion between the segments. The insets show blow-ups of the tail of the curves with the same x-axis scaling, showing exponential decay of the interaction energy. Due to the increased interfacial area for larger diameter rods, the strain present in the 6 nm rods is greater than that in the 4.8 nm diameter rods, resulting in larger elastic energies. For very small separations, the elastic energy in Fig. 4 is lowered, which will be explained when we examine the nature of the repulsive interaction (see below).

Strain fields, created by the lattice mismatch at the interface, decay both into the CdS regions and Ag_2S segments. Therefore, just as the elastic energy decreases
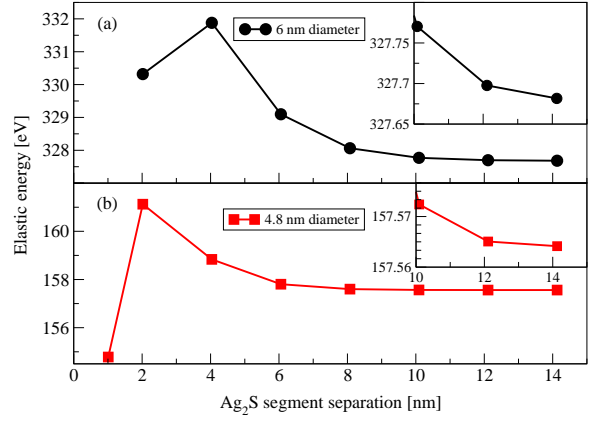

FIG. 4: (color online) Elastic energies of CdS nanorod superlattices containing two Ag_2S segments calculated with the VFF model. (a) 6 nm diameter nanorod, (b) 4.8 nm diameter nanorod. The energies decay with growing separation showing the elastic interaction between Ag_2S segments.

with the length of the CdS regions separating the two CdS-Ag_2S interfaces, it also decreases with Ag_2S segment size. Thus, for a given number of segments, the elastic energy is minimized when the sizes of all CdS regions are maximal, and the adjacent Ag_2S segments are equidistant from each other. Similarly, the Ag_2S segments also have equal sizes, maximizing the separations between CdS-Ag_2S interfaces within the segments. Indeed, introducing asymmetry into the Ag_2S segment

TABLE III: Introducing asymmetry into the VFF calculations, the elastic energies (in eV) and sizes of two Ag_2S segments (in nm), with 4 nm separation. The growth of one segment at the expense of the other is energetically unfavorable.

Segment 1	Segment 2	Energy
4	4	158.83
3	5	159.25
2	6	160.49

sizes results in higher elastic energies. For instance, the results of VFF calculations for the 4.8 nm diameter rods, with two asymmetric Ag_2S segments is presented in Table III. This indicates that diffusion of Ag^+ ions and growth of one fully formed segment at the expense of another is energetically unfavorable. The lowest elastic energy is reached when all the segments in the nanorod have the same size. This is consistent with the experimental finding of spontaneous ordering of Ag_2S segments, as well as the narrow distribution of Ag_2S segment sizes.[15]

It should be noted that the resulting superlattice is a metastable structure. The lowest energy structure would consist of two regions, Ag_2S and CdS with a single interface, as this would minimize both the interface formation and strain energies. Such state however cannot be reached because once a segment is fully formed, diffusion

of Ag^+ ions will not lower the interfacial energy until the two segments fully merge. That, in turn, is unfavorable because of the repulsion between segments due to strain.
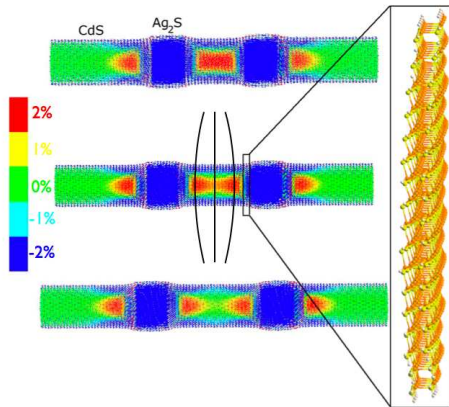

FIG. 5: (color online) Color maps of z-component of strain of the interatomic bonds, for the 4.8 nm diameter nanorod. The segment separations are 6, 8, 10 nm, the color map limits indicate strain of -2% (compression) to +2% (tension) for blue and red, respectively. The blow-up on the right shows two layers of CdS adjacent to the Ag_2S segment, illustrating CdS planes acquiring a convex shape. The atoms are pulled in opposite directions (indicated by the black lines at the center of the second rod), which leads to increased interaction energy when segments separation decreases.

To illustrate the elastic interaction between the two segments, we plot color coded maps of the z-component of the bond strain for the 4.8 nm diameter nanorod with segment separations of 6, 8, 10 nm, in Figure 5. The three nanorods demonstrate greater overlaps of z-strain with decreasing Ag_2S segment separation. The VFF relaxation predicts the 3D strain field resulting from the lattice mismatch at the interface. Although the full strain is a tensor field, the interaction can be demonstrated by looking at the z-axis strain fields. The red regions between the segments, decay away from the segment indicating that the interatomic bonds are stretched in the z-direction, with such distortion increasing toward the central axis of the rod. This results in overall deformation of CdS interatomic layers in the xy plane from flat to convex, as demonstrated by a two layer CdS cutout in Figure 5. Since the central xy plane must be flat, the deformations exemplified by the curved planes create competing forces, as schematically shown in Figure 5, resulting in a repulsive interaction.

This model also explains why for small separations between Ag_2S segments, i.e. below 4 nm for 6 nm diameter rods, and below 2 nm for 4.8 diameter rods the elastic energy actually decreases (Fig. 4). This is due to the fact that strains in z-direction created by the two neighboring segments are the result of bonds stretched in opposite directions. However, the $x-y$ direction stretching from the two segments match each other, for small segment separations. This cooperation lowers the strain energy and leads to an energy decrease at small segment separations as shown in Figure 4.

It is important to note that our VFF calculations for a variety of lattice mismatched hybrid nanorod structures indicate that such strain-mediated repulsive interaction is a general effect. For a pair of lattice mismatched materials, it is always present in nanostructures, resulting in energy curves similar to the ones in Figure 4, and should play an important part in the formation of lattice mismatched hybrid nanostructures.

IV. CONCLUSIONS

In this work, we have performed an analysis of the structural and elastic properties of the recently synthesized CdS-Ag_2S nanorod superlattices. Using experimental XRD data, we deduce the lattice geometry for the epitaxial attachment of monoclinic Ag_2S and wurtzite CdS. Using first principles methods, we calculate the formation energy of the CdS-Ag_2S interface, which indicates Ostwald ripening during the initial stages of Ag_2S nucleation and growth. A simple model of Ag^+ diffusion shows that the Ag_2S islands will condense into a number of segments, rather than divide a rod into two (or a few) large segregated parts of Ag_2S and CdS. This model also shows that during diffusion-limited growth of the Ag_2S islands can only lead to partial ordering and cannot account for the observed ordered structures alone. The epitaxial attachment of Ag_2S and CdS in the nanorod leads to significant amounts of strain due to a significant lattice mismatch. Our VFF calculations show that this results in significant elastic repulsion between neighboring Ag_2S segments. This interaction due to strain is likely crucial to the formation of nanorod superlattices since it can lead to spontaneous ordering of Ag_2S segments. This should be a general effect in evolution of chemically transformed nanostructures, i.e. similar repulsive interactions will always exist wherever there is a mismatch between components in a hybrid nanostructure.

V. ACKNOWLEDGMENTS

[1] Y. Wu, R. Fan, and P. Yang, Nano Letters **2**, 83 (2002).

[2] M. T. Björk, B. J. Ohlsson, T. Sass, A. I. Persson, C. The-

lander, M. H. Magnusson, K. Deppert, L. R. Wallenberg, and L. Samuelson, Nano Letters **2**, 87 (2002).

[3] M. S. Gudiksen, L. J. Lauhon, J. Wang, D. C. Smith, and C. M. Lieber, Nature **415**, 617 (2002).

[4] M. Achermann, M. A. Petruska, S. Kos, D. L. Smith, D. D. Koleske, and V. I. Klimov, Nature **429**, 642 (2004).

[5] I. Gur, N. A. Fromer, M. L. Geier, and A. P. Alivisatos, Science **310**, 462 (2005).

[6] D. J. Milliron, S. M. Hughes, Y. Cui, L. Manna, J. Li, L.-W. Wang, and A. P. Alivisatos, Nature **430**, 190 (2004).

[7] L. Ouyang, K. N. Maher, C. L. Yu, J. McCarty, and H. Park, J. Am. Chem. Soc. **129**, 133 (2007).

[8] V. A. Shchukin and D. Bimberg, Reviews of Modern Physics **71**, 1125 (1999).

[9] R. Nötzel, Semiconductor Science and Technology **11**, 1365 (1996).

[10] M. S. Miller, J.-O. Malm, M.-E. Pistol, S. Jeppesen, B. Kowalski, K. Georgsson, and L. Samuelson, Journal of Applied Physics **80**, 3360 (1996).

[11] G. Capellini, M. D. Seta, F. Evangelisti, V. A. Zinovyev, G. Vastola, F. Montalenti, and L. Miglio, Physical Review Letters **96**, 106102 (2006).

[12] Q. Xie, A. Madhukar, P. Chen, and N. P. Kobayashi, Physical Review Letters **75**, 2542 (1995).

[13] J. Tersoff, C. Teichert, and M. G. Lagally, Physical Review Letters **77**, 1675 (1996).

[14] T. Vicsek, Phys. Rev. Lett. **53**, 2281 (1984).

[15] R. D. Robinson, B. Sadtler, D. O. Demchenko, C. K. Erdonmez, L.-W. Wang, and A. P. Alivisatos, Science **317**, 355 (2007).

[16] G. Kresse and J. Furthmüller, Computational Materials Science **6**, 15 (1996).

[17] PEtot (Parallel Total Energy) Density Functional Code, URL http://hpcrd.lbl.gov/~linwang/PEtot/PEtot.html.

[18] A. Williamson, L. Wang, and A. Zunger, Physical Review B **62**, 12963 (2000).

[19] D. H. Son, S. M. Hughes, Y. Yin, and A. P. Alivisatos, Science **306**, 1009 (2004).

[20] E. M. Chan, M. A. Marcus, S. Fakra, M. ElNaggar, R. A. Mathies, and A. P. Alivisatos, J. Phys. Chem. A p. in print (2007).

[21] T. D. Dzhafarov, M. Serin, D. Ören, B. Süngü, and M. S. Sadigov, Journal of Physics D: Applied Physics **32**, L5 (1999).

[22] H. H. Woodbury, Physical Review **134**, A492 (1964).

[23] H. Schmalzried, Progress in Solid State Chemistry **13**, 119 (1980).

[24] S. Kashida, N. Watanabe, T. Hasegawa, H. Iida, M. Mori, and S. Savrasov, Solid State Ionics **158**, 167 (2003).

[25] P. Junod, H. Hediger, B. Kilchör, and J. Wullschleger, Philosophical Magazine **36**, 941 (1977).

[26] G. Kästner and U. Gösele, Philosophical Magazine **84**, 3803 (2004).

[27] E. Ertekin, P. A. Greaney, D. C. Chrzan, and T. D. Sands, J. Appl. Phys. **97**, 114325 (2005).

[28] M. C. Cross and P. C. Hohenberg, Rev. Mod. Phys. **65**, 851 (1993).

[29] V. Castets, E. Dulos, J. Boissonade, and P. D. Kepper, Phys. Rev. Lett. **64**, 2953 (1990).

[30] H. T. Dobbs, D. D. Vvedensky, A. Zangwill, J. Johansson, N. Carlsson, and W. Seifert, Phys. Rev. Lett. **79**, 897 (1997).

[31] Y. Chen and J. Washburn, Phys. Rev. Lett. **77**, 4046 (1996).

[32] P. Ravindran, L. Fast, P. A. Korzhavyi, B. Johansson, J. Wills, and O. Eriksson, Journal of Applied Physics **84**, 4891 (1998).

[33] J. A. Corll, Phys. Rev. **157**, 623 (1967).

[34] C. Pryor, J. Kim, L. W. Wang, A. J. Williamson, and A. Zunger, Journal of Applied Physics **83**, 2548 (1997).

[35] L. W. Wang and J. Li, Physical Review B **69**, 153302 (2004).